Letters in Nonlinear Analysis and its Applications **2** (2024) No. 2, 62-77
https://doi.org/10.66147/lnaa.20242229
Available online at www.lettersinnonlinearanalysis.com
**Research Article**

Letters in Nonlinear Analysis and its Applications
*Peer Review Scientific Journal*
**ISSN: 2958-874x**

# Computational analysis of Stagnation point flow of kerosine oil based hybrid Nanofluids over a porous plate comprising Radiation effect

Fatima Ali[a], Islam Zari[a], Tahir Saeed Khan[a], Karlygash Dosmagulova[b,c,d,*], Adnan Khan[a]

[a] *Department of Mathematics, University of Peshawar, Pakistan*
[b] *Institute of Mathematics and Mathematical Modeling, Almaty, Kazakhstan*
[c] *Al-Farabi Kazakh National University, Almaty, 050040, Kazakhstan*
[d] *Ghent University, Ghent, 9000, Belgium*

## Abstract

Numerous researchers worldwide have reported on the search for reliable methods to relate heat transfer to stagnation point flows. This paper studies the Hiemenz flow of a recently evolved hybrid nanofluid over a porous surface. To achieve the desired surface properties, kerosene oil is infused with nanoparticles of aluminum oxide and copper. Further, heat transfer due to isothermal radiation flux and dissipation by vicious means is examined. Supervising boundary value problems (BVPs) consist of partial differential equations (PDEs) which are transformed into ordinary differential equations (ODEs) through suitable similarity transformations. Infinite series solutions are obtained by the semi-analytic Homotopy analysis method (HAM), whereas numerical estimations are also conducted using the *bvp4c* collocation code. The software used to obtain the above solutions is MATHEMATICA and MATLAB, respectively. A graphical and tabular representation of the effects of parameter variations on dimensionless velocity, temperature, skin friction coefficient, and Nusselt number is included. It is found that the radiation parameter enhances

---

[*] Corresponding author

*Email addresses:* `fatimaalikhan1995.fak@gmail.com` (Fatima Ali), `zarimaths@uop.edu.pk` (Islam Zari), `tsk7@uop.edu.pk` (Tahir Saeed Khan), `karlygash.dosmagulova@ugent.be` (Karlygash Dosmagulova), `16adnan@stu.edu.cn` (Adnan Khan)

*Received December 5, 2023, Accepted: June 3, 2024, Online: June 15, 2024*

convection. Moreover, the injection significantly improves surface drag measures of kerosene-based hybrid nano-oil, while suction at the surface positively affects heat transfer and improves it. Despite that, the rise in the porosity factor diminishes the drag coefficient range.

*Keywords:* Hybrid nanofluids, $Al_2O_3 + Cu+$ Kerosene oil, Simulation, Stagnation point flow, Porous surface
*2010 MSC:* 80A10, 80A20, 76D55

## 1. Introduction

Viscous flows in the immediate neighborhood of the stagnation point are always evident when a solid body is immersed, suspended, or moving through an unbounded fluid. First and foremost, Hiemenz [1] presented the two-dimensional idea of such flows while studying the momentum boundary layer (MBL) formed. He elaborated on the flow formulation when the aqua medium impinges on a cylinder externally and MBL is evolved about a point of stagnation. Later, the problem was extended by numerous researchers by taking into account various physical attributes, since there are several applications today that require quick heat transfer and rapid cooling mechanisms involving stagnation region flows of thermally conducting fluids. For instance, such implementations happen in various fields of engineering, such as thermal, industrial, biological, mechanical, and many more. Yet, the low thermal conductivity of regular fluids (such as water, ethylene-glycol mixtures, and engine oils) is one of the many challenges faced by numerous heat exchange processes.

Considering the vanishing energy supply, nanofluid, a notable initiation of nanotechnology, has garnered a great deal of attention and appreciation as a heat-transferring fluid. These evolved mediums are defined as stable suspensions of conventional base fluids and nanomaterials, which are regarded as solid chemical particles manufactured with at least one dimension between $1 - 100\,nm$ [2]. By utilizing the theory of Maxwell, Eastman et al. [3] introduced nanofluids and, for the very first time, experimentally proved dramatic improvements in thermal conductivity and pressure drops of fluids. Thus, nanoscience has established a very broad base due to enhancing the thermal conductance in heat-conducting mechanisms, such as microfluidics, microelectronics, biomedicines, aerodynamics, nuclear systems, and many more [4]. The morphology of nano-additives may be different based on their chemical composition, and they are generally classified into carbides, nitrides, metal oxides, and carbon materials. However, the type, size, shape, chemical structure, and concentration are significant factors that affect obtaining optimistic conclusions. While studying the transportation of $Al_2O_3 + H_2O$ through a permeable domain, Shah et al. [5] also examined the effects of the shape factor of alumina nanoparticles, as a result of which they concluded that stronger convection is caused by a higher shape factor. Yu et al. [6] investigated the heat transfer effectiveness of kerosene-oil-based nanoliquid corresponding to $Fe_3O_4$ nanoparticles, as a result, they came up with optimal consequences of adding $Fe_3O_4$ to kerosene oil. On behalf of their profuse appreciation of science and technology, nanofluid flows have been crucially scrutinized by many researchers using numerous selections of nanomaterials and base fluids (Newtonian and non-Newtonian) while considering a diverse class of physical geometries (like planar, axisymmetric, spherical, cylindrical, and pipe channels), see [7]−[14].

Presently, hybrid nanofluids, which are colloids made of two nanomaterials combined with base fluids, have become extremely popular in recent years. Besides the conductive efficiency, hybrid nanofluids also have very fascinating and economic-friendly characteristics in heat exchangers, grinding machines, metal fabrication industries, and nuclear boiler temperature reductions [15]. [16] examined the flow of ethylene glycol loaded with the magnetite ($Fe_3O_4$) plus copper $Cu$ nanoadditives in a porous medium and ended up with a conclusion that $Fe_3O_4$ prizes high heat transfer rates in the shrinking case as compared to stretching state. Recently, Zari et al. [17] discussed the efficiency of water-based nanoliquid ($Al_2O_3 - Cu/H_2O$) within the stagnation neighborhood of stretching Riga plate, where they found great compatibility among alumina and copper oxide. It is noteworthy that alumina $Al_2O_3$ nanoparticles are extensively in demand due to their optimal heat capacities, chemical nobility, ceramic characteristics, and compatibility with each other. The supremacy of $Al_2O_3$ nanoparticles was significantly narrated by Farhana et al. [18] because of their engrossing stability and attributes. Notwithstanding, the low thermal conductance of $Al_2O_3$ nanoparticles can not be ignored. Thus, the compatibility of $Al_2O_3$ and $Cu$ nanoparticles suggest their hybrid nanoliquids as the best heat carrier fluids. This statement is marked positive by Devi and Devi [19] who studied $Cu - Al_2O_3/H_2O$ hybrid nanofluid flow past a stretching boundary, where they deduced thermal efficiency. The governing model formulated by them is mostly adopted for studying heat transfer through mono as well as hybrid nanofluid flows. Using $Al_2O_3 + Cu/H_2O$ hybrid nanofluid, Khatun et al. [20] implemented electromagnetic actuator and studied the heat transfer phenomena under isothermal radiation, while Zainal et al. [21] scrutinize the flow with thermal means of viscous dissipation.

In various fields of applied science, modern-day researchers are persuaded to explore the engrossing behaviors of visco-elastic conducting nanoliquids within stagnation regions of the Darcy-Forchheimer channels, since the increasing porosity and permeability, along with the inclusion of nanoparticles, has major impacts regarding the nanofluid dynamics in these loci [22]. Moreover, porosity refers to the presence of small pores on a surface, which permits externally present fluids, such as air, and water particles, to pass through the pores. A porous material is designed to have a large surface area and be lightweight to occupy fluid molecules. Based on the dimensions on which they are fabricated, these materials are grouped under the category of either macroporous, mesoporous, or microporous. Keeping in mind the significance of carbon nanotubes (CNTs), the Darcy-Forchheimer flow of water-based single-walled (SWCNTs) and multi-walled (MWCNTs) nanofluids gushed by a rotating disk was investigated by Nasir et al. [23], where the contributors came up with depletion in motion and thermal measures of $H_2O$ as increasing inertia coefficient and porosity parameter. Recently, Zari et al. [24], [25] carried out their analysis of kerosene-based nano-oil in the presence of CNTs (SWCNTs and MWCNTs) and deduced that the kerosene oil-based nanofluids can optimistically perform engrossingly in heat engines, nuclear vessels, and fuel involved practices. Rasool and the authors [26] comprehensively investigated the non-Darcian, electromagnetic, and hydrothermal flow of $Al_2O_3 + H_2O$ nanofluid over a convective Riga actuator (EMHD source), where they adopted the Buongiorno's two-phased approach that incorporated Brownian motion and thermophoresis effects. Likewise, Rasool et al. [27] carried out the investigation regarding a magnetohydrodynamic streaming of $Cu + Al_2O_3/H_2O$ across a penetrable shrinking surface in combination with ohmic and viscous dissipation, where they summarized dual solution for the flow problem when the suction restriction lies within a certain range. Porous medium may be manipulated for meteoric thermal transport and cooling [28]−[33].

In the context of heat flux modeled problems, several research works are to be had inside the literature on nanofluids with wonderful variables and amazing systematic tactics. However, to the exceptional of the authors' information, no endeavor has yet been taken to utilize the porous surface with radiation for this kind of flow setup. For the maximum of the instances, the researchers undertake to cope with the flow phenomena, regarding an outside free flow movement or transferring plates while, the incentive of the proposed studies describing is to look at the fluid flow generated with the aid of the porous phenomenon. Thus, a mathematical version for two-dimensional Heimenz flow towards a stretching porous plate in a kerosene oil-based hybrid nanofluid is examined whilst viscous dissipation, thermal radiation, suction, and injection are constructed and solved through the HAM to understand the above-mentioned flow phenomenon. In addition, a comparative evaluation between Water based hybrid nanofluids and Kerosene oil-based hybrid nanofluids is also part of the proposed research work.

## 2. Flow description

An incompressible stream of kerosene-based hybrid nanofluid loaded with $Al_2O_3$ and $Cu$ particles, fabricated at the nanoscale, moving towards a radiated porous sheet is analyzed here. The surface is implemented with suction while heat transfer is scrutinized under the effects of viscous dissipation. In this study, the plate is assumed to be isothermally radiated under conditions $T_w > 0$ and $T_w > T_\infty$. Heat transfer is also observed under the influence of viscous dissipation. Furthermore, let the velocity and temperature of the free stream be denoted as $U_\infty > 0$ and $T_\infty$, respectively. Above the boundary layer, velocity is assumed linear as well and defined as $u_e(x) = U_\infty x$. Along with this, isotropic flow fields and the state of thermal

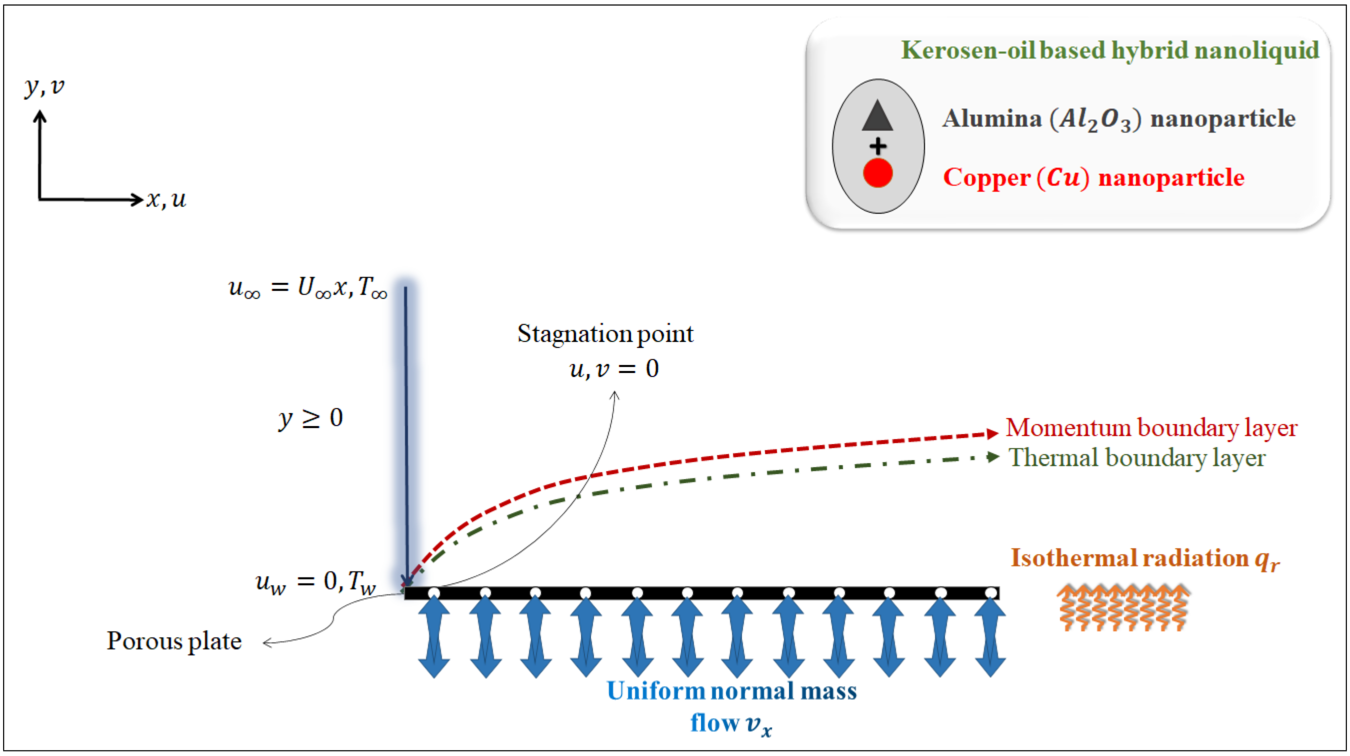

Figure 1: Physical illustration of Hiemenz flow towards an isothermally radiated porous plate in Cartesian $xy-$plane ([9, 33]).

equilibrium are taken into account. The physical schematic of the-described flow is given in Figure (1).

### *2.1. Governing model*

Taking two-dimensional boundary layer approximations into account, the presumed transport phenomenon is mathematically described with the help of the Hiemenz formulation and heat conduction equation (the way processed by [17, 19, 22, 24]) is defined so:

$$\frac{\partial u}{\partial x} + \frac{\partial v}{\partial y} = 0, \tag{1}$$

$$u\,\frac{\partial u}{\partial x} + v\,\frac{\partial u}{\partial y} = u_e\,\frac{du_e}{dx} + \frac{\mu_{hnf}}{\rho_{hnf}}\,\frac{\partial^2 u}{\partial y^2} - \nu_{hnf}\,\frac{u}{K}, \tag{2}$$

$$u\,\frac{\partial T}{\partial x} + v\,\frac{\partial T}{\partial y} = \alpha_{hnf}\,\frac{\partial^2 T}{\partial y^2} - \frac{1}{(\rho c_p)_{hnf}}\left(\frac{\partial q_r}{\partial y}\right) + \frac{\mu_{hnf}}{(\rho c_p)_{hnf}}\left(\frac{\partial u}{\partial y}\right)^2, \tag{3}$$

where $\langle u, v\rangle$ directs the velocity components in respective $(x, y)$ directions, $T$ symbolizes the absolute temperature distribution within relative boundary layers, whereas $\rho$ denotes the density field, and $K$ is the Darcian permeability of the plate. The subscript $_{hnf}$ indicates the corresponding properties of a hybrid nanofluid. Besides, $\nu_{hnf} = \frac{\mu_{hnf}}{\rho_{hnf}}$ and $\alpha_{hnf} = \frac{k}{(\rho c_p)_{hnf}}$ characterize the momentum and thermal diffusivity in eq. (2) and (3), sequentially. The symbol $v_w$ is also used to represent the uniform and normal suction velocity at the plate. Meanwhile, the eq. (1)−(3) are constrained to the Dirichlet boundary conditions:

$$\begin{cases} (\text{at } y = 0) \Rightarrow u = 0, \quad v = v_w \quad T = T_w, \\ (\text{as } y \to \infty) \Rightarrow u \to U_\infty\, x, \quad T \to T_\infty, \end{cases} \tag{4}$$

which are also signified as fixed boundary conditions in applied sciences. The constraints at $y = 0$ show the no-slip condition and heated fixed boundary, while the ones as $y \to \infty$ indicate the open end of the flow channel. Further proceeding with the well-known Rosseland approximation [17, 20, 34], the thermal radiation flux $q_r$ approximates as:

$$q_r = -\frac{4\,\sigma^*}{3\,\kappa^*}\,\frac{\partial T^4}{\partial y}, \tag{5}$$

where $\sigma^*$ and $\kappa^*$ present the Stefan-Boltzman constant and mean absorption coefficient, respectively. Linearizing $T^4$ with the help of Taylor expansion about $T_\infty$, which gives $T^4 \approx 4\,T_\infty^3\,T - 3\,T_\infty^4$, eq. (3) leads to:

$$u\,\frac{\partial T}{\partial x} + v\,\frac{\partial T}{\partial y} = \frac{k_{hnf}}{(\rho c_p)_{hnf}}\left(1 + \frac{k_f}{k_{hnf}}\,\frac{4}{3}\,R\right)\frac{\partial^2 T}{\partial y^2} + \frac{\mu_{hnf}}{(\rho c_p)_{hnf}}\left(\frac{\partial u}{\partial y}\right)^2 \tag{6}$$

where $R = 4\,T_\infty^3\left(\dfrac{\sigma^*}{k_f\,\kappa^*}\right)$ signifies the radiation parameter. The physical characteristics of prime consideration involve skin-friction coefficient $C_f$ and local Nusselt number $Nu_x$,

$$C_f = \frac{\tau_w}{\rho_f\,U_\infty^2}, \qquad \text{where} \qquad \tau_w = \mu_{hnf}\left(\frac{\partial u}{\partial y}\right)_{y=0}, \tag{7}$$

$$Nu_x = -\frac{x\,q_w}{k_f\,T_\infty\,(\theta_w - 1)}, \qquad \text{where} \qquad q_w = -\left(k_{hnf}\,\frac{\partial T}{\partial y} - q_r\right)_{y=0}. \tag{8}$$

In eqs. (7) and (8), $\tau_w$, $q_w$, and $q_r$ signify the surface shear stress, thermal flux, and radiative flux accordingly.

### 2.2. *Thermo-physical properties*

Moreover, the solicitousness thermo-physical properties appreciated here are density, dynamic viscosity, heat capacity, and thermal conductivity. From [9, 17, 24], relations of the-said properties for $Al_2O_3 + Cu$/Kerosene hybrid nanoliquid follow like:

$$\rho_{hnf} = (1 - \varphi_{s2})\big[(1 - \varphi_{s1})\rho_f + \varphi_{s1}\rho_{s1}\big] + \varphi_{s2}\rho_{s2}, \tag{9}$$

$$\mu_{hnf} = \big[(1 - \varphi_{s1})\,(1 - \varphi_{s2})\big]^{-2.5} \times \mu_f, \tag{10}$$

$$(\rho c_p)_{hnf} = (1 - \varphi_{s2})\big[(1 - \varphi_{s1})(\rho c_p)_f + \varphi_{s1}(\rho c_p)_{s1}\big] + \varphi_{s2}(\rho c_p)_{s2}, \tag{11}$$

$$k_{hnf} = \frac{k_{s2} + 2k_{nf} - 2\varphi_{s2}(k_{nf} - k_{s2})}{k_{s2} + 2k_{nf} + \varphi_{s2}(k_{nf} - k_{s2})} \times k_{nf}, \tag{12}$$

where

$$k_{nf} = \frac{k_{s1} + 2k_f - 2\phi_{s1}(k_f - k_{s1})}{k_p + 2k_f + \phi_{s1}(k_f - k_{s1})} \times k_f, \tag{13}$$

accordingly, whereas the numeric data is summarized in Table (1).

### 2.3. *Similarity transformation*

As implemented by Waini et. al. [9] to enforce the requirement that the resulting differential equation be independent of $\eta$, consider the suitable similarity variables,

$$\eta = \left(\frac{U_\infty}{\nu_f}\right)^{\frac{1}{2}} y, \quad \psi = (U_\infty\,\nu_f)^{\frac{1}{2}}\,x\,f(\eta), \quad \theta(\eta) = \frac{T - T_\infty}{T_w - T_\infty}, \tag{14}$$

where $\nu_f = \frac{\mu_f}{\rho_f}$ reflects the kinematic viscosity of kerosene oil and $\psi$ denotes the stream function. The path was initiated by Illingworth (1950), who found that it was convenient to account for viscosity and density

Table 1: Thermo-physical properties of kerosene oil, alumina ($Al_2O_3$), and copper ($Cu$) [9, 17, 24].

| **Properties and units:** | **Kerosene**<br>$f$ | $\mathbf{Al_2O_3}$<br>$s1$ | **Cu**<br>$s2$ |
|---|---|---|---|
| $\rho(kg\,m^{-3})$ | 783.0 | 3970.0 | 8933.0 |
| $c_p(J\,kg^{-1}\,K^{-1})$ | 2090.0 | 765.0 | 385.0 |
| $k(W\,m^{-1}\,K^{-1})$ | 0.145 | 40 | 400 |
| Prandtl number, $Pr$ | 21 | – | – |

effects in terms of similarity variable $\eta$. By the use of eq. (14), the dimensionless velocity components and temperature follow as:

$$u = U_\infty\, x\, f'(\eta), \quad v = -(U_\infty\, \nu_f)^{\frac{1}{2}}\, f(\eta), \quad T = T_\infty\left[1 + \theta(\eta)\,(\theta_w - 1)\right]. \tag{15}$$

In the light of eqs. (14)−(15), continuity eq. (1) evidently satisfies. Further, the rest of eqs. (2), (6) and (4) reduce to:

$$A_1\, f''' + A_2\left[f\, f'' - f'^2 + 1\right] - A_1\, A_2\, \gamma\, f' = 0, \tag{16}$$

and

$$H\,\theta'' + Pr\left[A_3\, f\,\theta' + A_1\, Ec\, f''^2\right] = 0, \tag{17}$$

subjected to:

$$\begin{cases}(at \quad \eta = 0) \Rightarrow \quad f(0) = \alpha^*,\ f'(0) = 0,\ \theta(0) = 1,\\ (as \quad \eta \to \infty) \Rightarrow \quad f'(\infty) \to 1,\ \theta(\infty) \to 0,\end{cases} \tag{18}$$

where primes denote differentiation with respect to $\eta$. Here, the significant ratios are denoted as:

$$A_1 = \frac{\mu_{hnf}}{\mu_f}, A_2 = \frac{\rho_{hnf}}{\rho_f}, A_3 = \frac{(\rho c_p)_{hnf}}{(\rho c_p)_f}, A_4 = \frac{k_{hnf}}{k_f}, H = A_4\left(1 + \frac{1}{A_4}\,\frac{4}{3}\,R\right), \tag{19}$$

which are defined with the help of eqs. (9)−(12). Besides, the dimensionless description of $C_f$ and $Nu_x$ results:

$$(Re_x)^{\frac{1}{2}} C_f = A_1\, f''(0), \quad (Re_x)^{-\frac{1}{2}}\, Nu_x = -H\,\theta'(0). \tag{20}$$

Here,

$$\begin{cases}\alpha^* = -\dfrac{v_w}{(U_\infty\,\nu_f)^{\frac{1}{2}}}, \quad \gamma = \dfrac{1}{U_\infty\, K}, \quad R = 4\, T_\infty^3\left(\dfrac{\sigma^*}{k_f\,\kappa^*}\right),\\ Ec = \dfrac{(u_e)^2}{(c_p)_f\, T_\infty\,(\theta_w - 1)}, \quad Pr = \dfrac{(\mu\, c_p)_f}{k_f}, \quad Re_x = \left(\dfrac{u_w\, x}{\nu_f}\right), \quad \theta_w = \dfrac{T_w}{T_\infty}.\end{cases} \tag{21}$$

In eq. (21), $\alpha^*$, $R$, $Ec$, $\gamma$, $Pr$, $Re_x$, and $\theta_w$ are the suction/injection parameter, radiation parameter, Eckert number, porosity factor, Prandtl number, local Reynolds number, and temperature ratio parameter, sequentially. Note that $\alpha^*$, also called the mass transfer coefficient, is such that $\alpha^* > 0$ shows suction process, $\alpha^* < 0$ denotes corresponding injection effect, while $\alpha^* = 0$ represents an impermeable surface.

## 3. Solution schemes

The derived dimensionless prototype, involving eqs. (16)−(18), is handled analytically (via the homotopy analysis method) and numerically (with the help of *bvp4c*) as well.

### *3.1. Analytic solution: HAM*

The homotopy analysis method (HAM) is a recently developed semi-analytic technique that is based on the fundamental concepts of topological structures, known as homotopy [35]. It generates a series solution, that may be infinite or truncated up to some sufficient order, for boundary value problems (BVPs), using the Homotopy-Maclaurins series. The beauty of HAM lies in the convergence of its solutions. It gives excellent flexibility to the expression of the solution and provides great freedom in choosing the base functions of the desired solution and the corresponding auxiliary linear operator of homotopy. As demonstrated by [8, 17, 24, 36, 37], we select a set of initial guesses,

$$f_0(\eta) = e^{-\eta} - 1 + \alpha^* + \eta, \quad \theta_0(\eta) = e^{-\eta}, \tag{22}$$

meeting (18) and auxiliary linear operators,

$$\mathcal{L}_f[f] = f''' - f', \qquad \mathcal{L}_\theta[\theta] = \theta'' - \theta, \tag{23}$$

accordingly, so that

$$\mathcal{L}_f\left[a_1 + a_2\, e^{\eta} + a_3\, e^{-\eta}\right] = 0, \quad \mathcal{L}_\theta\left[a_4\, e^{\eta} + a_5\, e^{-\eta}\right] = 0, \tag{24}$$

for integral constants $\{a_i \text{ for } i = 1, \cdots, 5\}$. For continuous homotopy maps $\tilde{f}[\eta;p] : f_0(\eta) \sim f(\eta)$ and $\tilde{\theta}[\eta;p] : \theta_0(\eta) \sim \theta(\eta)$, contemplate $p$, $\hbar_f$, $\hbar_\theta$ showing the embedding parameter and non-trivial convergence-control variables, respectively. Then, the *zeroth*-order deformation problems are formulated as:

$$(1-p)\,\mathcal{L}_f\left[\tilde{f}(\eta;p) - f_0(\eta)\right] = p\,\hbar_f\,\mathcal{N}_f\left[\tilde{f}(\eta;p)\right], \tag{25}$$

$$(1-p)\,\mathcal{L}_\theta\left[\tilde{\theta}(\eta;p) - \theta_0(\eta)\right] = p\,\hbar_\theta\,\mathcal{N}_\theta\left[\tilde{f}(\eta;p), \tilde{\theta}(\eta;p)\right], \tag{26}$$

$$\text{bound to:}\begin{cases}\tilde{f}(0;p) = \alpha^*, \quad \tilde{f}_\eta(0;p) = 0, \quad \tilde{\theta}(0;p) = 1,\\ \tilde{f}_\eta(\infty;p) = 1, \quad \tilde{\theta}(\infty;p) = 0,\end{cases} \tag{27}$$

with non-linear operators written from eqs. (16) and (17) like:

$$\mathcal{N}_f\left[\tilde{f}(\eta;p)\right] = \frac{A_1}{A_2}\,\tilde{f}_{\eta\eta\eta} - \left(\tilde{f}_\eta^2 - \tilde{f}\,\tilde{f}_{\eta\eta} - 1 + \gamma\,A_1\,\tilde{f}_\eta\right) = 0, \tag{28}$$

$$\mathcal{N}_\theta\left[\tilde{f}(\eta;p), \tilde{\theta}(\eta;p)\right] = H\,\tilde{\theta}_{\eta\eta} + Pr\,A_3\,\tilde{f}\,\tilde{\theta}_\eta + Pr\,Ec\,A_1\,\tilde{f}_{\eta\eta}^2 = 0. \tag{29}$$

Note that $p \in [0,1]$ and $\tilde{f}$ and $\tilde{\theta}$ continually deform from initial to final solutions as $p$ grows within $[0,1]$,

$$\tilde{f}(\eta;0) = f_0(\eta), \quad \tilde{f}(\eta;1) = f(\eta), \quad \text{and} \quad \tilde{\theta}(\eta;0) = \theta_0(\eta), \quad \tilde{\theta}(\eta;1) = \theta(\eta). \tag{30}$$

Similarly, introducing definitions,

$$f_m(\eta) = \frac{1}{m\,!}\,\frac{\partial^m \tilde{f}(\eta;p)}{\partial p^m}\Big|_{p=0}, \quad \text{and} \quad \theta_m(\eta) = \frac{1}{m\,!}\,\frac{\partial^m \tilde{\theta}(\eta;p)}{\partial p^m}\Big|_{p=0}, \tag{31}$$

cast the *mth*-order deformation problems so:

$$\mathcal{L}_f\left[f_m(\eta) - \chi_m\, f_{m-1}(\eta)\right] = \hbar_f\,\mathcal{R}_m^f(\eta), \tag{32}$$

$$\mathcal{L}_\theta\left[\theta_m(\eta) - \chi_m\,\theta_{m-1}(\eta)\right] = \hbar_\theta\,\mathcal{R}_m^\theta(\eta), \tag{33}$$

$$\text{subject to:}\begin{cases}f_m(0) = \alpha^*, \quad f_m'(0) = 0, \quad f_m'(\infty) = 0,\\ \theta_m(0) = 0, \quad \theta_m(\infty) = 0,\end{cases} \tag{34}$$

where

$$\mathcal{R}^{f}_{m}\left(\eta\right)=\frac{A_1}{A_2}\,f'''_{m-1}-\left[\sum_{n=0}^{m-1}\left[f'_n\,f'_{(m-1-n)}-f_n f''_{(m-1-n)}\right]-(1-\chi_m)+\gamma\,A_1\sum_{n=0}^{m-1}f'_{m-1-n}\right], \tag{35}$$

$$\mathcal{R}^{\theta}_{m}\left(\eta\right)=H\,\theta''_{m-1}+Pr\,A_3\sum_{n=0}^{m-1}f_{m-1-n}\theta'_n+Pr\,Ec\,A_1\sum_{n=0}^{m-1}f''_{m-1-n}f''_n, \tag{36}$$

by using eqs. (28) and (29). Also, here $m \geq 1$ and

$$\chi_m=\begin{cases}0, & m\leq 1\\ 1, & m>1\end{cases} \tag{37}$$

By processing *bvph*2.0 code according to above statements, MATHEMATICA generates the infinite homotopy-series solutions,

$$f\left(\eta\right)=f_0(\eta)+\sum_{n=1}^{+\infty}f_n(\eta),\quad \text{and}\quad \theta\left(\eta\right)=\theta_0(\eta)+\sum_{n=1}^{+\infty}\theta_n(\eta), \tag{38}$$

and consequently *mth*-order approximation follows:

$$f\left(\eta\right)\approx f_0(\eta)+\sum_{n=1}^{m}f_n(\eta),\quad \text{and}\quad \theta\left(\eta\right)\approx\theta_0(\eta)+\sum_{n=1}^{m}\theta_n(\eta). \tag{39}$$

### *3.2. Numerical solution*

Besides analytic, eqs. (16)−(18) are investigated numerically also. *bvp4c* solver code via MATLAB mathematical tool is being adopted, see [9, 24, 37, 38]. This uses a collocation method (CM) and processes the Lobatto IIIa formula. Beginning with, let the collocation variables:

$$f=Y(1),f'=Y(2),f''=Y(3),\theta=Y(4),\theta'=Y(5). \tag{40}$$

Eq. (40), the dimensionless supervising model transforms into a system of first-order ODEs as:

$$\begin{cases}Y'(1)=Y(2),\\ Y'(2)=Y(3),\\ Y'(3)=\dfrac{A_2}{A_1}\left[Y(2)^2-Y(1)\,Y(3)-1+\gamma\,A_1\,Y(2)\right],\\ Y'(4)=Y(5),\\ Y'(5)=-\dfrac{Pr}{H}\left[A_3\,Y(1)\,Y(5)+Ec\,A_1\,Y(3)^2\right]\end{cases} \tag{41}$$

$$\text{exposed to:}\begin{cases}Y_0(1)=\alpha^*,\quad Y_0(2)=0,\quad Y_0(4)=1, & \text{(at surface, }\eta=0)\\ Y_\infty(1)\to 1,\quad Y_\infty(4)\to 0, & \text{(at free-stream, }\eta\to\infty).\end{cases} \tag{42}$$

MATLAB engenders a collocation polynomial that interpolates $C^1$−continuous solution within the provided mesh data.

## 4. Ramifications and discussions

Various physical parameters have major consequences for non-dimensional characteristics and are given prime consideration in this section. Accordingly, they include $\alpha^*$, $\gamma$, $R$, $Ec$ and associated $\phi$ of both nanoparticles. The results on dimensionless velocity and temperature fields ($f'(\eta)$ and $\theta(\eta)$) against essential parameters are elucidated in Figures (2)−(11), sequentially, while the after-effects upon $(Re_x)^{\frac{1}{2}}C_f$ and $(Re_x)^{-\frac{1}{2}}Nu_x$ are provided in Tables (3) and (4). The Figures are obtained via analytic solutions whereas the computations in Tables are conducted from numerical estimations.

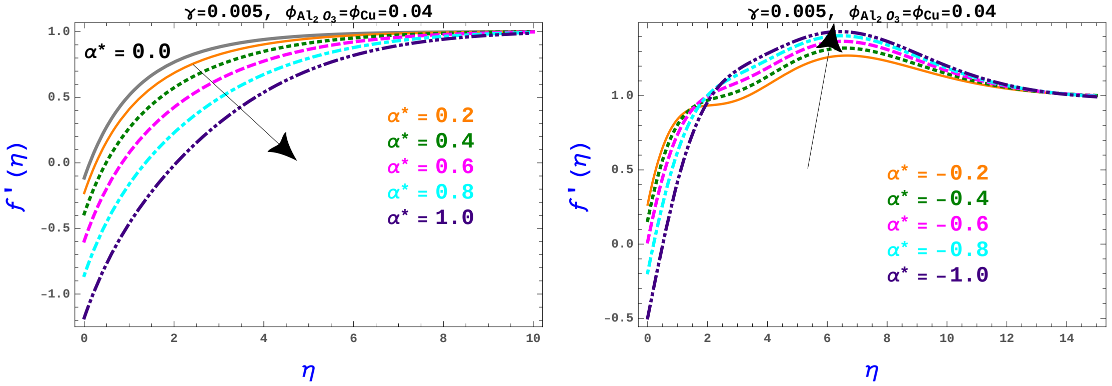

(a) Suction $\alpha^* > 0$.

(b) Injection $\alpha^* < 0$.

Figure 2: Effects against variations in suction/injection parameter $\alpha^*$ upon velocity profile $f'(\eta)$.

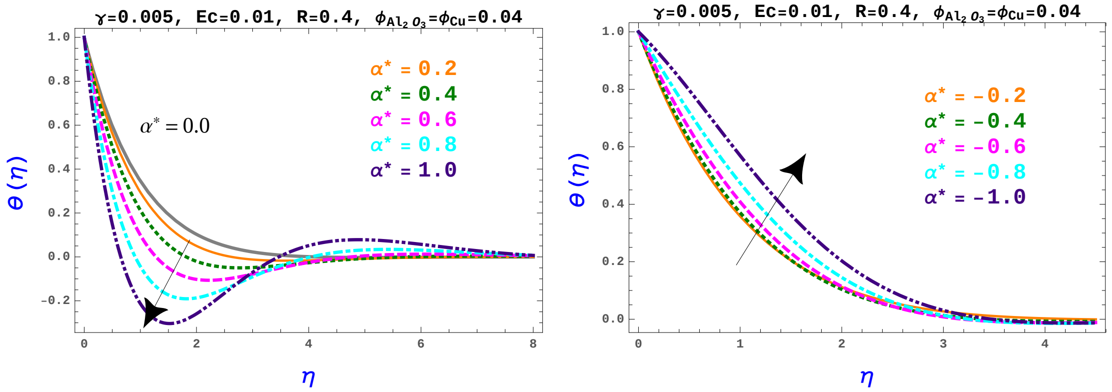

(a) Suction $\alpha^* > 0$.

(b) Injection $\alpha^* < 0$.

Figure 3: Effects against variations in suction/injection parameter $\alpha^*$ upon temperature profile $\theta(\eta)$.

### *4.1. Analysis of velocity and temperature profiles*

Figures (2) and (3) illustrate the upshots regarding velocity and temperature profiles against suction/injection parameters, simultaneously. From Figure (2a), it is noticed that an upsurge in the magnitude of $\alpha^*$ causes a significant downward shift in the velocity distribution within the momentum boundary layer region. This is obvious because suction tends the heated fluid towards the surface wall where the buoyancy forces result from retardation in the motion of molecules. Likewise, decreasing patterns are reported for $\theta(\eta)$, as demonstrated in Figure (3a). However, opposite patterns are observed for both velocity and temperature distribution under the injection process, as illustrated in Figures (2b) and (3b), respectively.

From Figures (4) and (5), the most important transpositions in $f'(\eta)$ and $\theta(\eta)$ against $\gamma$ are evident. Figure (4) narrates that for increasing ranges of porosity, there are increments in velocity. These constructive influences can be physically explained because an increase in porosity increases the capacity for fluid to flow. Notwithstanding, improvements within the thermal boundary layer are obtained for climbing values of $\gamma$, as shown in Figure (5). Schematics (7)−(9) inform the major alterations in motion and heat transfer of the hybrid nanofluid caused by $\phi_{Cu}$ and $\phi_{Al_2O_3}$. These plots explain destructive and adverse behaviors in $f'(\eta)$ for increasing measures of solid volume concentration of both nanoparticles. This fact further explicates the increments in the temperature of the boundary layer. However, alumina nanoparticles have a greater effect on the said quantities compared to copper nanoparticles. The preceding observations are crystal clear from Figures (7)−(9).

Moreover, the after-effects of radiation parameter $R$ and Eckert number $Ec$ are plotted in Figures

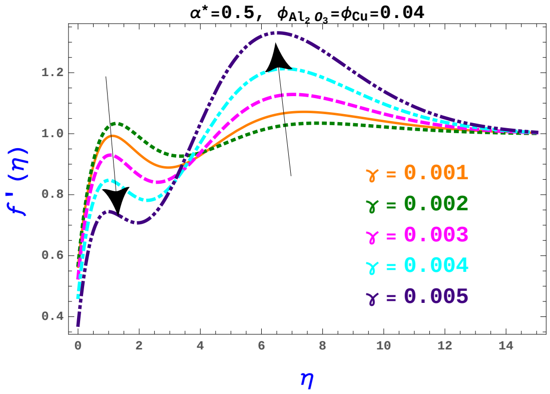

Figure 4: Effects against variations in porosity factor $\gamma$ upon velocity profile $f'(\eta)$.

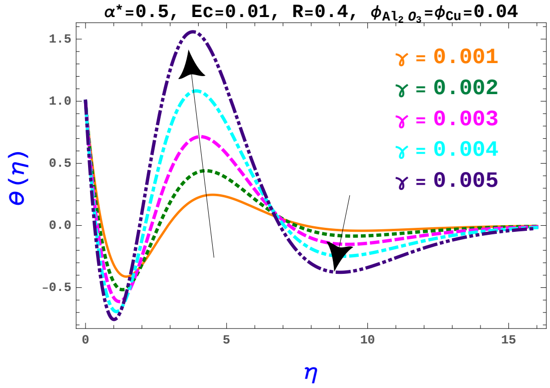

Figure 5: Effects against variations in porosity factor $\gamma$ upon temperature profile $\theta(\eta)$.

(10) and (11), respectively. $R$ has quite captivating properties in heat transfer. Thermal radiation occurs at electromagnetic wavelengths, whose absorbing powers make this form of heat transport so appealing. Consequently, the temperature is greatly affected and gradually decreases. Finally, the last Figure (11) illustrates the adverse effects associated with $\theta(\eta)$ under increasing $Ec$.

### *4.2. Numerical results*

As a result of *bvp4c*, the computations obtained are displayed in Table (3) and (4). The former shows the variation in $(Re_x)^{\frac{1}{2}}C_f$ and $(Re_x)^{-\frac{1}{2}}Nu_x$ regarding injection ($\alpha^* < 0$), non-permeability ($\alpha^* = 0$), and suction ($\alpha^* < 0$) at the surface wall. On the other hand, Table (4) is constructed that file the outcomes caused by variant adaptations for $Pr$, $\gamma$, $R$, $Ec$, $\phi_{Al_2O_3}$, and $\phi_{Cu}$ upon preceding physical quantities, simultaneously for the case of suction ($\alpha^* = 0.15$).

Table 2: Comparative check of numerical code corresponding to $Pr = 6.2$ and trivial concentration of nanostructures in the base fluid in accord with $\gamma = \alpha^* = R = Ec = 0.0$

| | **Base fluid** | **Nanomaterial** | $f''(0)$ | $-\theta'(0)$ |
|---|---|---|---|---|
| Bachok et al. [7] | Water | $Cu$ | 1.127510821 | – |
| Waini et al. [9] | Water | $Al_2O_3 + Cu$ | 1.232588 | – |
| Zari et al. [17] | Water | $Al_2O_3 + Cu$ | 1.232493957 | 1.127510821 |
| **Present evaluations** | Kerosene | $Al_2O_3 + Cu$ | 1.230844936 | 1.127202097 |

Firstly, Table (2) frames the code check by analyzing the reliability of the proposed model through a comparison made for the estimations of $f''(0)$ and $-\theta'(0)$. For this, the nanostructure's concentration

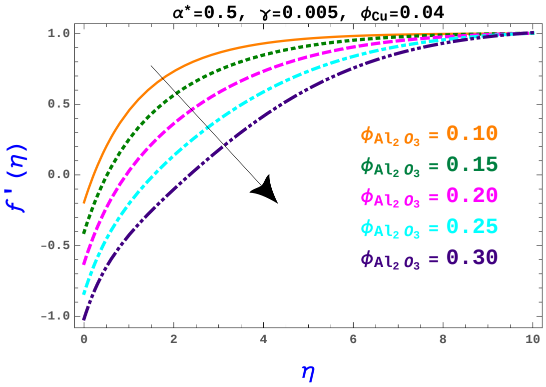

Figure 6: Effects against variations in volume fraction of alumina nanoparticles $\phi_{Al_2O_3}$ upon velocity profile $f'(\eta)$.

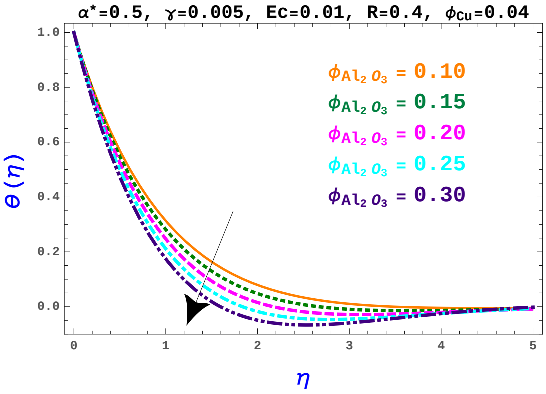

Figure 7: Effects against variations in volume fraction of alumina nanoparticles $\phi_{Al_2O_3}$ upon temperature profile $\theta(\eta)$.

is taken to zero, the Prandtl number is set to 21 while the rest of the parameters are also valued trivial ($\gamma = \alpha^* = R = Ec = 0.0$), in accordance with the articles [7, 9, 17]. Table (2) shows considerable agreement with the previously available literature.

Table 3: Variations in non-dimensional skin friction and Nusselt number under altering suction/injection parameter $\alpha^*$, while $Pr = 21$, $\gamma = 1.0$, $R = 0.3$, $Ec = 0.01$, and $\phi_{Al_2O_3} = \phi_{Cu} = 0.02$.

| $\alpha^*$ | $(Re_x)^{\frac{1}{2}}C_f$ | $(Re_x)^{-\frac{1}{2}}Nu_x$ |
|---|---|---|
| **Injection $\alpha^* < 0$** | | |
| $-1.0$ | 0.674074475 | $-0.005461216$ |
| $-0.5$ | 0.830806332 | $-0.011932952$ |
| $-0.3$ | 0.904166896 | 0.072958726 |
| $-0.2$ | 0.943158900 | 0.328923491 |
| $-0.1$ | 0.983678630 | 0.937529577 |
| **Non-permeability $\alpha^* = 0$** | | |
| 0.0 | 1.025707511 | 1.991268346 |
| **Suction $\alpha^* > 0$** | | |
| 0.1 | 1.069218247 | 3.442437584 |
| 0.2 | 1.114181167 | 5.173691638 |
| 0.3 | 1.160566144 | 7.077939121 |
| 0.5 | 1.257409327 | 11.150380032 |
| 1.0 | 1.520985427 | 21.819987499 |

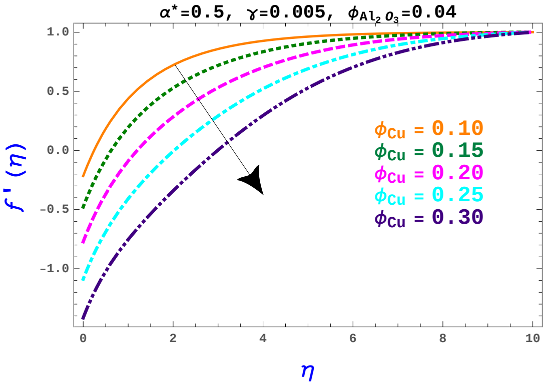

Figure 8: Effects against variations in volume fraction of copper nanoparticles $\phi_{Cu}$ upon velocity profile $f'(\eta)$.

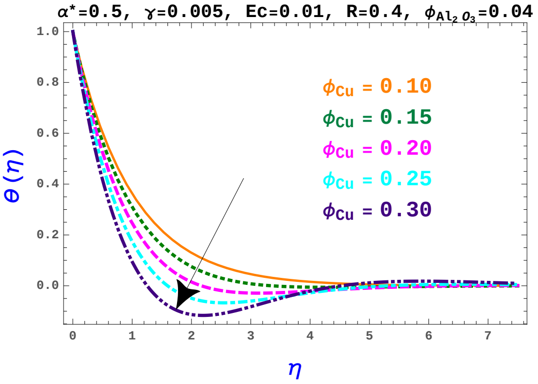

Figure 9: Effects against variations in volume fraction of copper nanoparticles $\phi_{Cu}$ upon temperature profile $\theta(\eta)$.

From Table (3), it is clearly observed that the increasing injection parameter ($\alpha^* < 0$) causes decreasing patterns in skin friction and local Nusselt number, although, negative values are recorded relative to the latter quantity. Physiologically, this implies that the imbuing scenario shows the backflow of the thermal gradients in opposition to surface-shear drag which diminishes and as a result accelerates the fluid flow. On the other hand, $(Re_x)^{\frac{1}{2}}C_f$ and $(Re_x)^{-\frac{1}{2}}Nu_x$ portray increasing patterns as the value of suction parameter $\alpha^* > 0$ goes high. Since the Nusselt number is the ratio of convection to heat transfer by conduction, the above statements conclude that the convection eventually gets escalated while the fluid motion faces retardation under shoot-ups in the suction/injection parameter. Moreover, note that the variations regarding surface friction are very gradual and cautious, however, the changes in the local Nusselt number are monotonic and sudden.

Table (4) is calculated to observe the impacts on $(Re_x)^{\frac{1}{2}}C_f$ and $(Re_x)^{-\frac{1}{2}}Nu_x$ against changing values of $Pr$, $\gamma$, $R$, $Ec$, $\phi_{Al_2O_3}$, and $\phi_{Cu}$ while keeping $\alpha^* = 0.15$. It is noticed that $Pr$ significantly influences convective heat transfer and enhances it as compared to the conductive process. In terms of porosity, improvements are observed related to both $(Re_x)^{\frac{1}{2}}C_f$ and $(Re_x)^{-\frac{1}{2}}Nu_x$ for higher values of $\gamma$. Further, Table (4) narrates that the volume fraction of both nanoparticles has chief ramifications on the skin friction coefficient and Nusselt number. Having strong values of $\phi_{Al_2O_3}$ and $\phi_{Cu}$, $(Re_x)^{\frac{1}{2}}C_f$ reflects destructive responses, while a significant constructive notion is perceived in the measures of $(Re_x)^{-\frac{1}{2}}Nu_x$. Besides, from Table (4), it is also noticed that the incremented ranges of $R$ are favorable for heat transfer rates, rather than $Ec$ which adversely affects it and weakens the fluid convection. Meanwhile, it is noteworthy that the effects of $R$ and $Ec$ are recorded on a minimal level and have no measurable effect on the overall counts.

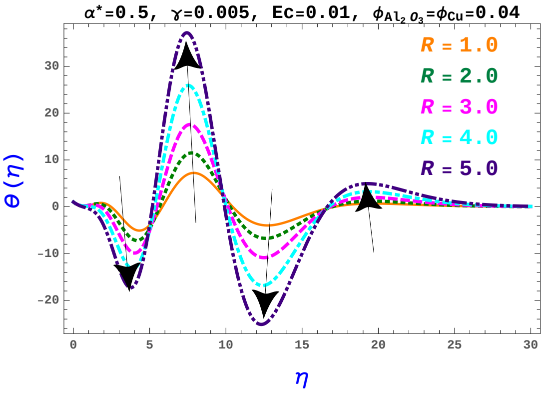

Figure 10: Effects against variations in radiation parameter $R$ upon temperature profile $\theta(\eta)$.

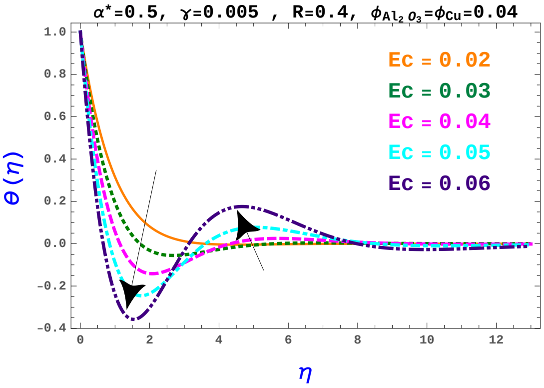

Figure 11: Effects against variations in Eckert number $Ec$ upon temperature profile $\theta(\eta)$.

## 5. Final findings

Ongoing work reports on the study of the stagnation point flow of $Al_2O_3 + Cu$+kerosene hybrid nano-oil towards a porous medium that is being isothermally heated. Furthermore, the heat transfer is examined in combination with radiative and viscous dissipation is taken into account. The transport phenomenon is mathematically described by the Hiemenz formulation and energy equation susceptible to the Dirichlet boundary conditions. This governing model consists of a partial differential system which is reduced to an ordinary differential notion via a set of similarity transformations. The problem is solved analytically and numerically using HAM and CM, accordingly. We examine the influence of paramount parameters on momentum and thermal diffusivity within the relative boundary layer. Based on all the discussions and observations, the key conclusions that emerge as a result are as follows:

- Injection responds to significant positive impacts on kerosene-based hybrid nano-oil, whereas heat transfer exhibits enhanced performance under the suction process.
- Regarding the addition of both copper and alumina nanoparticles, thermal transportation is speeded up, although the medium is slowed down correspondingly.
- In addition, the overall consequences associative to $Cu$ nanoparticles on velocity and temperature are substantially stronger than those of $Al_2O_3$ nanoparticles.
- Increasing the porosity factor indicates enhanced outcomes for both the flow and thermal measures. However, the final impressions on heat transfer are quite encouraging.
- The temperature profile is positively affected by intensifying radiation parameters. As a result, these major impacts provide unparalleled benefits for heat transfer.

Table 4: Variations in non-dimensional skin friction and Nusselt number under altering the values of sundry parameters, while $\alpha^* = 0.15$.

| $Pr$ | $\gamma$ | $R$ | $Ec$ | $\phi_{Al_2O_3}$ | $\phi_{Cu}$ | $(Re_x)^{\frac{1}{2}}C_f$ | $(Re_x)^{-\frac{1}{2}}Nu_x$ |
|---|---|---|---|---|---|---|---|
| 6.3 | 1.0 | 0.3 | 0.01 | 0.02 | 0.02 | 1.091519161 | 1.997658382 |
| 13.0 | | | | | | 1.091519557 | 3.153485664 |
| 21.0 | | | | | | 1.091521296 | 4.421189808 |
| 30.0 | | | | | | 1.091519447 | 5.804351403 |
| 21.0 | 0.8 | 0.3 | 0.01 | 0.02 | 0.02 | 1.163692207 | 4.461352691 |
| | 1.4 | | | | | 0.973264062 | 4.347356081 |
| | 2.0 | | | | | 0.843436839 | 4.250458566 |
| | 2.6 | | | | | 0.750653316 | 4.164945652 |
| 21.0 | 1.0 | 0.5 | 0.01 | 0.02 | 0.02 | 1.091521283 | 4.682080843 |
| | | 0.7 | | | | 1.091519564 | 4.924877163 |
| | | 0.9 | | | | 1.091519557 | 5.153555412 |
| | | 1.1 | | | | 1.091519552 | 5.370977676 |
| 21.0 | 1.0 | 0.3 | 0.02 | 0.02 | 0.02 | 1.091521297 | 4.355744732 |
| | | | 0.04 | | | 1.091521299 | 4.224854631 |
| | | | 0.06 | | | 1.091521299 | 4.093964482 |
| | | | 0.08 | | | 1.091521289 | 3.963073460 |
| 21.0 | 1.0 | 0.3 | 0.01 | 0.1 | 0.02 | 1.356574176 | 5.108863229 |
| | | | | 0.2 | | 1.752047660 | 5.992436646 |
| | | | | 0.3 | | 2.256650047 | 6.912289873 |
| | | | | 0.4 | | 2.935877939 | 7.880664195 |
| 21.0 | 1.0 | 0.3 | 0.01 | 0.02 | 0.1 | 1.570379128 | 5.258703492 |
| | | | | | 0.2 | 2.228270458 | 6.322473900 |
| | | | | | 0.3 | 3.028842731 | 7.428895808 |
| | | | | | 0.4 | 4.077341945 | 8.596312056 |

- The thermal convection is adversely affected for higher values of Eckert number, while conduction mechanisms improve.
- Moreover, the suction/injection parameter has much more influence on the local Nusselt number in comparison to the skin friction coefficient.
- Based on Table (3), the suction phenomenon at the surface positively affects heat transfer in opposition to the injection scenario.
- In the view of Table (4), the heat transfer coefficient appears to show boost-ups compared to increments in the radiation parameter as opposed to the rising values of the Eckert number, which causes the local Nusselt number to fall down.
- In spite of that, the upsurge in porosity factor diminishes the range of drag coefficient, in the view of Table (4).
- It is hoped that all these results will be beneficial for rapid cooling and heat exchange processes involving porous surfaces.

## References

[1] Hiemenz, K., The boundary layer on a straight circular cylinder immersed in the uniform flow of liquid, *Dinglers Polytech. J.*, **(1911)**, 326, 321-324.

[2] Baig, N.; Kammakakam, I.; Falath, W., Nanomaterials: a review of synthesis methods, properties, recent progress, and challenges, *Adv. Mater.*, **(2021)**, 2, 1821-1871.

[3] Eastman, J. A.; Choi, U. S., Li, S., Thompson, L. J.; Lee, S., Enhanced thermal conductivity through the development of nanofluids, *MRS Online Proceedings Library (OPL)*, **(1996)**, 457.

[4] Jana, S.; Salehi-Khojin, A.; Zhong, W. H., Enhancement of fluid thermal conductivity by the addition of single and hybrid nano-additives, *Thermochim. Acta*, **(2007)**, 462, 45-55.

[5] Shah, Z.; Babazadeh, H.; Kumam, P.; Shafee, A.; Thounthong, P., Numerical simulation of magnetohydrodynamic nanofluids under the influence of shape factor and thermal transport in a porous media using CVFEM, *Front. Phys.*, **(2019)**, 7, 164.

[6] Yu, W.; Xie, H.; Chen, L.; Li, Y., Enhancement of thermal conductivity of kerosene-based $Fe_3O_4$ nanofluids prepared via phase-transfer method, *Colloids Surf. A Physicochem. Eng. Asp.*, **(2010)**, 355, 109-113.

[7] Bachok, N.; Ishak, A.; Nazar, R.; Senu, N., Stagnation-point flow over a permeable stretching/shrinking sheet in a copper-water nanofluid, *Bound. Value Probl.*, **(2013)**, 2013, 1-10.

[8] Shafiq, A.; Zari, I.; Khan, I.; Khan, T. S.; Seikh, A. H.; Sherif, E. S. M., Marangoni-driven boundary layer flow of carbon nanotubes toward a Riga plate, *Front. Phys.*, **(2020)**, 7, 215.

[9] Waini, I.; Ishak, A.; Pop, I, Hiemenz flow over a shrinking sheet in a hybrid nanofluid, *Results Phys.*, **(2020)**, 19, 103351.

[10] Shah, N. A.; Wakif, A.; El-Zahar, E. R.; Ahmad, S.; Yook, S. J., Numerical simulation of a thermally enhanced EMHD flow of a heterogeneous micropolar mixture comprising (60%)-ethylene glycol (EG),(40%)-water (W), and copper oxide nanomaterials ($CuO$), *Case Stud. Therm. Eng.*, **(2022)**, 35, 102046.

[11] Oreyeni, T.; Shah, N. A.; Popoola, A. O.; Elzahar, E. R.; Yook, S. J., The significance of exponential space-based heat generation and variable thermophysical properties on the dynamics of Casson fluid over a stratified surface with non-uniform thickness, *Waves. Random. Complex. Media.*, **(2022)**, 1-19.

[12] Rasool, G.; Shah, S. Z. H.; Sajid, T.; Jamshed, W.; Cieza Altamirano, G.; Keswani, B.; Sánchez-Chero, M., Spectral Relaxation Methodology for Chemical and Bioconvection Processes for Cross Nanofluid Flowing around an Oblique Cylinder with a Slanted Magnetic Field Effect, *Coatings*, **(2022)**, 12, 1560.

[13] Batool, S.; Rasool, G.; Alshammari, N.; Khan, I.; Kaneez, H.; Hamadneh, N., Numerical analysis of heat and mass transfer in micropolar nanofluids flow through lid driven cavity: Finite volume approach, *Case Stud. Therm. Eng.*, **(2022)**, 37, 102233.

[14] Priyadharshini, P.; Archana, M. V.; Ahammad, N. A.; Raju, C. S. K.; Yook, S. J.; Shah, N. A., Gradient descent machine learning regression for MHD flow: Metallurgy process, *Int. Commun. Heat Mass Transf.*, **(2022)**, 138, 106307.

[15] Jamil, F.; Ali, H. M., Applications of hybrid nanofluids in different fields. In Hybrid nanofluids for convection heat transfer, *Academic Press.*, **(2020)**, 215-254.

[16] Eid, M. R.; Nafe, M. A., Thermal conductivity variation and heat generation effects on magneto-hybrid nanofluid flow in a porous medium with slip condition, *Waves. Random. Complex. Media.*, **(2022)**, 32, 1103-1127.

[17] Zari, I.; Ali, F.; Khan, T. S.; Shafiq, A., Radiative Hiemenz flow towards a stretching Riga plate in hybrid nanofluid, *Int. Commun. Heat Mass Transf.*, **(2022)**, 139, 106492.

[18] Farhana, K.; Kadirgama, K.; Rahman, M. M.; Noor, M. M.; Ramasamy, D.; Samykano, M.; Tarlochan, F., Significance of alumina in nanofluid technology, *J. Therm. Anal. Calorim.*, **(2019)**, 138, 1107-1126.

[19] Devi, S. U.; Devi, S. A., Heat transfer enhancement of $Cu-Al_2O_3$/water hybrid nanofluid flow over a stretching sheet, *J. Nigerian Math. Soc.*, **(2017)**, 36, 419-433.

[20] Khatun, S.; Islam, M. M.; Mollah, M. T.; Poddar, S.; Alam, M. M., EMHD radiating fluid flow along a vertical Riga plate with suction in a rotating system, *SN Appl. Sci.*, **(2021)**, 3, 1-14.

[21] Zainal, N. A.; Nazar, R.; Naganthran, K.; Pop, I., Viscous dissipation and MHD hybrid nanofluid flow towards an exponentially stretching/shrinking surface, *Neural. Comput. Appl.*, **(2021)**, 1-11.

[22] Khan, W. A.; Pop, I. M., Boundary layer flow past a stretching surface in a porous medium saturated by a nanofluid: Brinkman-Forchheimer model, **(2012)**.

[23] Nasir, S.; Shah, Z.; Islam, S.; Khan, W.; Bonyah, E.; Ayaz, M.; Khan, A., Three-dimensional Darcy-Forchheimer radiated flow of single and multiwall carbon nanotubes over a rotating stretchable disk with convective heat generation and absorption, *AIP Adv.*, **(2019)**, 9, 035031.

[24] Zari, I.; Shafiq, A.; Khan, T. S., Simulation study of Marangoni convective flow of kerosene oil based nanofluid driven by a porous surface with suction and injection, *Int. Commun. Heat Mass Transf.*, **2021**, 127, 105493.

[25] Zari, I.; Gul, T.; Dosmagulova, K.; Saee, T.; Haq, S, Heat transfer analysis of Radiative-Marangoni Convective flow in nanofluid comprising Lorentz forces and porosity effects, *Advances in the Theory of Nonlinear Analysis and its Applications*, **2023**, 7(1), 61-81.

[26] Rasool, G.; Wakif, A.; Wang, X; Shafiq, A.; Chamkha, A. J., Numerical passive control of alumina nanoparticles in purely aquatic medium featuring EMHD driven non-Darcian nanofluid flow over convective Riga surface, *Alex. Eng. J.*, **(2023)**, 68, 747-762.

[27] Rasool, G.; Wang, X.; Yashkun, U.; Lund, L. A.; Shahzad, H., Numerical treatment of Hybrid Water Based Nanofluid flow with Effect of Dissipation and Joule Heating Over a Shrinking Surface: Stability Analysis, *J. Magn. Magn.*, **(2023)**, 170587.

[28] Fuqiang, W.; Xinping, Z.; Yan, D.; Hongliang, Y.; Shi, X.; Yang, L.; Ziming, C., Progress in radiative transfer in porous medium: a review from macro scale to pore scale with experimental test, *Appl. Therm. Eng.*, **(2022)**, 118331.

[29] Omowaye, A. J.; Fagbade, A. I.; Ajayi, A. O., Dufour and soret effects on steady MHD convective flow of a fluid in a porous medium with temperature dependent viscosity: Homotopy analysis approach, *J. Niger. Soc. Math.*, **(2015)**, 34, 343-360.

[30] Alzahrani, A. K., Ullah, M. Z., Alshomrani, A. S.; Gul, T., Hybrid nanofluid flow in a Darcy-Forchheimer permeable medium over a flat plate due to solar radiation, *Case Stud. Therm. Eng.*, **(2021)** 26, 100955.

[31] Zubair, M.; Jawad, M.; Bonyah, E.; Jan, R., MHD Analysis of Couple Stress Hybrid Nanofluid Free Stream over a Spinning Darcy-Forchheimer Porous Disc under the Effect of Thermal Radiation, *J. Appl. Math.*, **(2021)**.

[32] Rasool, G.; Shah, N. A.; El-Zahar, E. R.; Wakif, A., Numerical investigation of EMHD nanofluid flows over a convectively heated riga pattern positioned horizontally in a Darcy-Forchheimer porous medium: Application of passive control strategy and generalized transfer laws, *Waves. Random. Complex. Media.*, **(2022)**, 1-20.

[33] Joshi, N.; Upreti, H.; Pandey, A. K., MHD Darcy-Forchheimer $Cu-Ag/H_2O-C_2H_6O_2$ hybrid nanofluid flow via a porous stretching sheet with suction/blowing and viscous dissipation, *Int. J. Comput. Methods Eng.*, **(2022)**, 1-9.

[34] Hosseinzadeh, K.; Asadi, A.; Mogharrebi, A. R.; Azari, M. E.; Ganji, D. D., Investigation of mixture fluid suspended by hybrid nanoparticles over vertical cylinder by considering shape factor effect, *J. Therm. Anal. Calorim.*, **(2021)**, 143, 1081-1095.

[35] Altaie, S. A.; Anakira, N.; Jameel, A.; Ababneh, O.; Qazza, A.; Alomari, A. K., Homotopy Analysis Method Analytical Scheme for Developing a Solution to Partial Differential Equations in Fuzzy Environment, *Fractal. Fract.*, **(2022)**, 6, 419.

[36] Zhao, Y.; Lin, Z.; Liao, S. A modified homotopy analysis method for solving boundary layer equations, *Appl. Math.* **(2013)**, 4, 11-15.

[37] Dinarvand, S., Nodal/saddle stagnation-point boundary layer flow of CuO-Ag/water hybrid nanofluid: a novel hybridity model, *Microsyst. Technol.*, **2019**, 25, 2609-2623.

[38] Kierzenka, J.; Shampine, L. F., A BVP solver that controls residual and error, *JNAIAM J. Numer. Anal. Ind. Appl. Math*, **(2008)**, 3, 27-41.